Topological Floquet engineering using two frequencies in two dimensions

Yixiao Wang,[1] Anne-Sophie Walter,[1] Gregor Jotzu,[2] and Konrad Viebahn[1,*]

[1] *Institute for Quantum Electronics, ETH Zurich, 8093 Zurich, Switzerland*
[2] *Max Planck Institute for the Structure and Dynamics of Matter, 22761 Hamburg, Germany*

(Dated: January 13, 2023)

Using two-frequency driving in two dimensions opens up new possibilites for Floquet engineering, which range from controlling specific symmetries to tuning the properties of resonant gaps. In this work, we study two-band lattice models subject to two-tone Floquet driving and analyse the resulting effective Floquet bandstructures both numerically and analytically. On the one hand, we extend the methodology of Sandholzer et al. [10.1103/PhysRevResearch.4.013056] from one to two dimensions and find competing topological phases in a simple Bravais lattice when the two resonant drives at 1ω and 2ω interfere. On the other hand, we explore driving-induced symmetry breaking in the hexagonal lattice, in which the breaking of either inversion or time-reversal symmetry can be tuned independently via the Floquet modulation. Possible applications of our work include a simpler generation of topological bands for ultracold atoms, and the realisation of non-linear Hall effects as well as Haldane's parity anomaly in inversion-symmetric parent lattices.

I. INTRODUCTION

Topological phenomena emerge naturally for electrons under the effect of strong magnetic fields, exemplified by the quantum Hall effect (QHE) [1]. In these phenomena, the underlying physical mechanism is the breaking of time-reversal symmetry due to the magnetic field. Several years after the discovery of the QHE it was noticed that topological insulators can also arise without an ambient magnetic field, such as the anomalous quantum Hall state [2] and the quantum spin Hall effect [3]. Today, anomalous topological phases can be realised by Floquet engineering, that is, periodic driving of a quantum system. So far, Floquet engineered topological phenomena have been largely limited to single-frequency protocols, applied to optical lattices [4–13], real materials [14–17], photonic and plasmonic waveguides [18–20], and other synthetic systems [21–24]. Recently, bichromatic and multi-frequency Floquet engineering has emerged as a powerful strategy to enhance the driving capabilities. These include time-reversal or spatial symmetry breaking [25–35] and interference between different Floquet harmonics [36–42]. The combination of both two-path interference and time-reversal symmetry breaking has led to the proposal [43] and experimental demonstration [44] of a topological pump in one-dimensional lattice. To our knowledge, all experimental results in the multi-frequency regime have been limited to one-dimensional driving patterns, motivating the need to find novel strategies for two-dimensional driving.

In this work, we use the idea of two-tone Floquet engineering to generate novel topological bandstructures and topological phase transitions from simple parent lattices in two dimensions. On the one hand, we consider resonant driving for the lowest two bands of a triangular lattice. Although this model only features a single potential minimum per unit cell, we are able to drive topological transitions by tuning the amplitude and relative phase between 1ω and 2ω drives. The simplicity of this scheme could open up new pathways for realising strongly correlated topological insulators, which have remained out of reach in existing methods. On the other hand, we apply two-frequency driving to an inversion-symmetric (graphene-like) hexagonal lattice. This driving scheme enables the selective breaking of inversion symmetry while maintaining time-reversal symmetry, giving access to a new class of Floquet Hamiltoninans. Thus, we find that an external breaking of inversion symmetry is not necessary to drive the celebrated parity anomaly in the Haldane model [2]. The two-frequency approach generically applies to Floquet-driven systems in lattices, ranging from condensed matter to synthetic quantum matter.

The remainder of this paper is structured as follows. The relevant two-tone driving waveforms, and possible experimental implementations, are introduced in section II. Afterwards, we show how resonant 1ω–2ω driving in a triangular lattice leads to topological phase transitions (section III). Section IV discusses the effective breaking of time-reversal and inversion symmetry under off-resonant driving in a hexagonal lattice.

II. 1ω–2ω FLOQUET DRIVING IN TWO DIMENSIONS

Two-frequency driving can be applied, in princple, to any physical system which has been employed for Floquet engineering so far [14]. As a generic starting point, we consider a particle confined to a static potential $V_{\mathrm{lat}}(r)$, and subject to an oscillating force

$$\hat{H}_{\mathrm{cm}}(\tau) = \frac{\hat{p}^2}{2m} + V_{\mathrm{lat}}(r) - \mathbf{F}(\tau)\cdot\hat{r}\ , \tag{1}$$

with

$$\mathbf{F}(\tau) \equiv e\mathbf{E}(\tau) = -m\ddot{\mathbf{r}}_m(\tau) = -\dot{\mathbf{A}}(\tau)\ . \tag{2}$$

* viebahnk@phys.ethz.ch

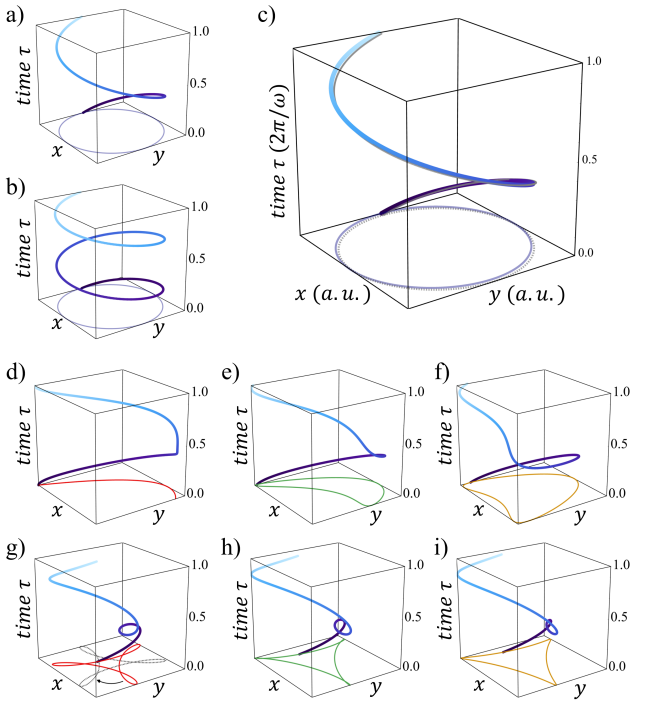

FIG. 1. Single- and two-frequency Lissajous curves for two-dimensional driving. The plots show the real-space modulation figures $\mathbf{r}_m(\tau)$ (Eq. 4). These shapes are topologically equivalent to those of the time-dependent force $\mathbf{F}(\tau)$, since the two are related to one another by taking the second derivative (Eq. 2). (a-c) Circular strong driving at 1ω (a), circular weak driving 2ω (b), or both drives combined (c) can be used to resonantly address a higher-band transition. The thin line in (c) represents the dominant 1ω waveform, the same as (a). (d-f) Superposition of an elliptical driving field at 1ω and a linear field at 2ω with relative phases $\varphi_{y1} = 0$ (d), 0.2π (e), and 0.5π (f). (g-i) Superposition of two circular drives with relative phase $\varphi_{x2} = 0.9\pi$, $\varphi_{y1} = 0.5\pi$, $\varphi_{y2} = 0.4\pi$, driving strength $K_{x2} = K_{y2} = 0.7$, and $K_{x1} = K_{y1} = 0.5$ (g), 0.65 (h), and 0.8 (i).

In solid state systems, the driving force $\mathbf{F}(\tau)$ can directly correspond to the oscillating field $\mathbf{E}(\tau)$ of a laser coupling to free electrons [17, 45]. Equivalently, the application of periodic driving can be seen as 'minimal coupling' using the vector potential as $q \to q - \mathbf{A}(\tau)/\hbar$. Furthermore, collective modes such as phonons [46] or magnons [47] can also be involved. In waveguide-based synthetic lattices, transverse movements of the waveguides provide an effective inertial force [19]. For optical lattices, the driving force can be provided by an oscillating optical or magnetic gradient [48]. Alternatively, an inertial force can result from a periodic displacement of the entire lattice potential, an approach known as 'lattice shaking' [4, 5]. In this case, the Hamiltonian in the lab frame is

$$\hat{H}_{\mathrm{lab}}(\tau) = \frac{\hat{p}^2}{2m} + V_{\mathrm{lat}}\left[r - \mathbf{r}_m(\tau)\right] \ , \tag{3}$$

related to Eq. 2 by two unitary transformations [49]. In summary, the derivations in this work directly carry over from engineered quantum platforms, such as ultracold atoms in optical lattices, to condensed matter systems.

We define the two-dimensional driving pattern $\mathbf{r}_m(\tau)$ as

$$\begin{aligned} x_m(\tau) = \quad & A_{x1}\cos(\omega\tau) \quad + A_{x2}\cos(2\omega\tau + \varphi_{x2}) \\ y_m(\tau) = & A_{y1}\cos(\omega\tau + \varphi_{y1}) + A_{y2}\cos(2\omega\tau + \varphi_{y2}) \ . \end{aligned} \tag{4}$$

These two-tone driving waveforms are visualised as Lissajous curves in Fig. 1 for the relevant choices of driving parameters (phases and amplitudes) used in this work. The amplitude of the vector potential is given by the dimensionless driving strength $K_{\alpha\beta} = m\omega_\beta A_{\alpha\beta} a/\hbar$, where a is the lattice spacing and $A_{\alpha\beta}$ is the real-space amplitude. The index $\alpha \in \{x, y\}$ denotes the direction, whereas $\beta \in \{1, 2\}$ indicates the frequency.

Resonant circular 1ω–2ω driving. The combination of a strong circular 1ω drive (Fig. 1a, $\varphi_{y1} = \pi/2$) with a weak circular 2ω drive (Fig. 1b, $\varphi_{x2} = 0$, $\varphi_{y2} = \pi/2$) leads to a modulated circular pattern (Fig. 1c). Due to two-path interference when addressing the s–p resonance of the triangular lattice, this driving pattern can be used to drive topological transitions in two dimensions, similar to the topological pump of ref. [44].

Off-resonant 1ω–2ω driving to access spatial and temporal symmetries. Alternatively, an elliptical driving field at 1ω and a linearly polarised laser at 2ω ($A_{x2} = 0, \varphi_{y2} = 0$) leads to a competition between the breaking of inversion symmetry and time-reversal symmetry. For instance, the choice $\varphi_{y1} = 0$ results in a 'boomerang' pattern (Fig. 1d), which breaks inversion symmetry but not time-reversal symmetry. Conversely, the case of $\varphi_{y1} = \pi/2$ (Fig. 1f) gives a rounded 'kite' shape in which the breaking of time-reversal symmetry dominates over the breaking of inversion symmetry. Tuning the phase φ_{y1} thus allows to interpolate between the two symmetry breaking situations (Fig. 1e), thereby accessing novel topological regimes.

Instead of combining linear and elliptical drives, the competition between inversion-breaking and time-reversal-breaking can be achieved by superimposing two circular drives of opposite helicity (Fig. 1g-i). The way in which inversion symmetry is broken in this case depends on the relative orientation of the driving pattern to the lattice geometry. This can be tuned by increasing φ_{x2} and φ_{y2} by the same amount (i.e. by delaying the two frequency drives with respect to each other), which rotates the driving pattern around the origin (Fig. 1g, see also refs. [29, 33, 34]). Driving a topological transition via changing only a relative phase can be experimentally advantageous in condensed matter systems where changing polarisation or amplitude can lead to spurious effects.

Experimental implementation. In this work we focus on a triangular and a hexagonal lattice. A corresponding optical lattice potential, and the resulting tight-binding parameters, can be found in Appendix A. In waveguide-based systems, the lattice geometry can generally be cho-

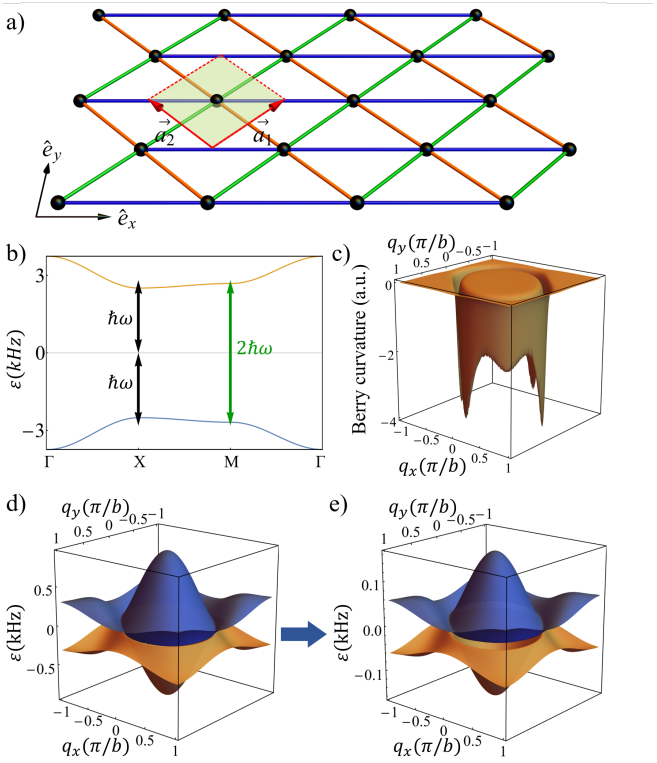

FIG. 2. Resonant band coupling in the triangular lattice (a), with relevant parameters $t_1 = -0.05$, $t_2 = -0.07$, $t_3 = -0.07$, $\varepsilon = -0.66$ in units of E_{rec} and dimensionless inter-band coupling $\eta_{sp} = 0.19$. Resonant one-photon or two-photon processes lead to the coupling of lower and higher bands, corresponding to the green and black arrows in (b), respectively. Floquet driving lifts the degeneracy of the static band structure in the rotating frame (c) and opens a band gap (d). The ring-shape minima of the band structure leads to a ring-shape Berry curvature (e). (f) shows a trivial spatially localized Berry curvature under two-frequency driving, which features a strong Berry curvature dipole.

sen freely [19]. The time-dependence of the driving term is encoded in an additional spatial coordinate, which can accommodate multi-frequency driving. Finally, in solid state systems, the laser field corresponding to the driving term at 2ω can be generated via second-harmonic generation, ensuring that it is phase-stable with respect to the 1ω term. The relative phase between the two can then be tuned using a dispersive material of varying thickness.

Tight-binding Hamiltonians for two-dimensional Floquet engineering. By expanding the original Hamiltonian (Eq. 1) in a Wannier basis and transforming it to quasimomentum space, we get the following expression

$$\sum_n \Big\{ \varepsilon_n \hat{a}_n^\dagger \hat{a}_n - \sum_{i=1}^{Z} \Big[t_{n,i} \left(e^{i(\theta_i(\tau)+\mathbf{q}\cdot\mathbf{b}_i)} \hat{a}_n^\dagger \hat{a}_n + h.c. \right) \Big] - \mathbf{F}(\tau)\cdot\hat{r} \sum_{n'} \eta_{nn'} \hat{a}_n^\dagger \hat{a}_{n'} \Big\} . \tag{5}$$

Here, ε_n, $t_{n,i}$, $\eta_{nn'}$ are the band centre energies, nearest-neighbour tunnelling matrix elements, and interband coupling elements, respectively, for bands n, n' (Appendix B). $\mathbf{b}_i = j\mathbf{a}_1 + k\mathbf{a}_2$ are the nearest-neighbour tunneling vectors and i indexes the in-equivalent neighbours up to the coordination number Z; $\mathbf{a}_1$, $\mathbf{a}_2$ correspond to the primitive translation vectors in two dimensions. The time-periodic Peierls phases are $\theta_i(\tau) = \frac{m}{\hbar}\mathbf{b}_i \cdot \dot{\mathbf{r}}_m(\tau)$. In second quantisation, $\hat{a}_n$ denotes the annihilation operator in band n. The first line of Eq. 5 describes static and time-dependent contributions to intra-band processes whereas the second line is the inter-band coupling that arises from periodically forcing the system. The coupling elements $\eta_{nn'}$ can be understood as dipole matrix elements of Bloch states [41]. Consequently, the first line is diagonal in quasimomentum and band index n, whereas the second line contributes off-diagonal elements to the Hamiltonian.

We use the Hamiltonian in Eq. 5 as the starting point for the Floquet analysis. If the periodic drive resonantly addresses the gap between s and p bands, we additionally employ a unitary transformation to 'rotate away' the energy difference (sec. III). In order to evaluate the effective Floquet Hamiltonian, we employ two complementary methods. On the one hand, we calculate the effective Hamiltonian analytically in inverse powers of the driving frequency ω using the well-known high-frequency expansion (HFE) [50–54]. Since we work in the weak driving regime the HFE remains valid. On the other hand, we can numerically obtain the effective Hamiltonian via the Trotter decomposition [55]. We use this numerical method to validate the results of the analytic calculation and to justify the truncation of the high-frequency expansion a posteriori. To characterise the band topologies, the Berry curvature is evaluated via the eigenstates in the discretised two-dimensional Brillouin zone. The resulting Chern number is the surface integral of the Berry curvature over the closed Brillouin torus [56, 57].

III. RESONANTLY DRIVEN TRIANGULAR LATTICE

The first situation we consider is a simple triangular lattice in which the lowest two bands (s and p) are resonantly coupled with two frequencies, inspired by ref. [43] and building on previous works using single-frequency driving [58–60].

In the non-shaken case the static Hamiltonian for a triangular tight-binding model is

$$\hat{H} = \left[\varepsilon + \sum_{i=1}^{3} t_i \cos(\mathbf{q}\cdot\mathbf{b}_i) \right] \sigma_z \ . \tag{6}$$

The nearest-neighbour tunneling vectors are $\mathbf{b}_1 = (-1,1)b$, $\mathbf{b}_2 = (1,0)b$, $\mathbf{b}_3 = (0,1)b$ and $\mathbf{q} = (q_x, q_y)$ in the rotated coordinate $\hat{e}'_x = \frac{\hat{e}_x+\hat{e}_y}{\sqrt{2}}$, $\hat{e}'_y = \frac{-\hat{e}_x+\hat{e}_y}{\sqrt{2}}$ (Fig. 2a). The simplest way to couple s and p bands is

to apply single-frequency driving, parametrised by Eq. 4 with $A_{x2} = A_{y2} = 0$ and denoting φ_{y1} as φ.

Starting from Eq. 5 the time-dependent Hamiltonian can be written as

$$\hat{H}(\tau) = \left\{ \varepsilon + \sum_{i=1}^{3} t_i \cos\left[\mathbf{q}\cdot\mathbf{b}_i + \theta_i(\tau)\right] \right\} \sigma_z + \left[\eta_{sp}\hbar\omega K_x \cos(\omega\tau) + \eta_{sp}\hbar\omega K_y \cos(\omega\tau+\varphi)\right]\sigma_x, \tag{7}$$

where $\varepsilon = (\varepsilon_s - \varepsilon_p)/2 = -\Delta\varepsilon/2$ with $\Delta\varepsilon$ being the gap size. The other parameters are $t_i = t_{s,i} - t_{p,i}$ with $i = 1,2,3$, the Peierls phases are $\theta_i(\tau) = -\frac{1}{\hbar}\int_0^\tau \mathbf{F}(\tau')\cdot\mathbf{b}_i\, d\tau' = -[K_x\sin(\omega\tau)\hat{x} + K_y\sin(\omega\tau+\varphi)\hat{y}]\cdot\mathbf{b}_i/b$, and the Pauli matrices are σ_j with $j = x,y,z$. The dimensionless driving strengths are denoted by $K_x = m\omega A_{x1}a/\hbar$, $K_y = m\omega A_{y1}a/\hbar$, respectively. The tight-binding parameters, including the tunneling amplitudes, inter-band coupling and band center energies, are obtained from a triangular lattice potential by evaluating the Wannier functions (Appendix B, Fig. 2a).

Single-frequency circular driving resonant with the gap. If the frequency ω is near-resonant with the gap, corresponding to the dominant one-photon process, we apply the unitary $\mathcal{U}_R(\tau) = \exp(-i\omega\tau\sigma_z/2)$ to eliminate the energy gap between the two bands (Fig. 2d). This gives

$$\hat{H}(\tau) = \left\{ \varepsilon + \hbar\omega/2 + \sum_{i=1}^{3} t_i \cos\left[\mathbf{q}\cdot\mathbf{b}_i + \theta_i(\tau)\right] \right\} \sigma_z + \left[\eta_{sp}\hbar\omega K_x \cos(\omega\tau) + \eta_{sp}\hbar\omega K_y \cos(\omega\tau+\varphi)\right] \times \left[\sigma_x\cos(\omega\tau) - \sigma_y\sin(\omega\tau)\right]/2. \tag{8}$$

The terms proportional to the identity matrix can be omitted without affecting the topology of the bands.

By analysing Eq. 8 in the high-frequency expansion (Appendix C), we find a ring-shaped gap opening (Fig. 2e, see also refs. [13, 61]). However, the off-diagonal terms are dominanted by constants. Physically, this corresponds to on-site couplings between the s and p bands, which yield topologically trivial bands (Fig. 3a).

Single-frequency elliptical driving resonant with half the gap. Driving the system at half the gap energy ($\hbar\omega = 12.8t_1 = 0.64E_{rec}$) leads to neighbouring-site interband couplings which can give rise to topological bands. Starting from the waveforms in Eq. 4 with $K_{x2} = K_{y2} = 0$ and applying the unitary $\mathcal{U}_R(\tau) = \exp(-i\omega\tau\sigma_z)$ gives

$$\hat{H}(\tau) = \left\{ \varepsilon + \hbar\omega + \sum_{i=1}^{3} t_i \cos\left[\mathbf{q}\cdot\mathbf{b}_i + \theta_i(\tau)\right] \right\} \sigma_z + \left[\eta_{sp}\hbar\omega K_x \cos(\omega\tau) + \eta_{sp}\hbar\omega K_y \cos(\omega\tau+\varphi)\right] \times \left[\sigma_x\cos(2\omega\tau) - \sigma_y\sin(2\omega\tau)\right]/2, \tag{9}$$

where $\varepsilon + \hbar\omega \approx 0$. In this case, the only non-zero Fourier components of the drive are $\pm1\omega$ and $\pm3\omega$. Contrary to the direct one-photon resonance, the inter-band couplings happen via two-photon processes (Fig. 2b). We now find quasimomentum-dependent σ_x and σ_y terms

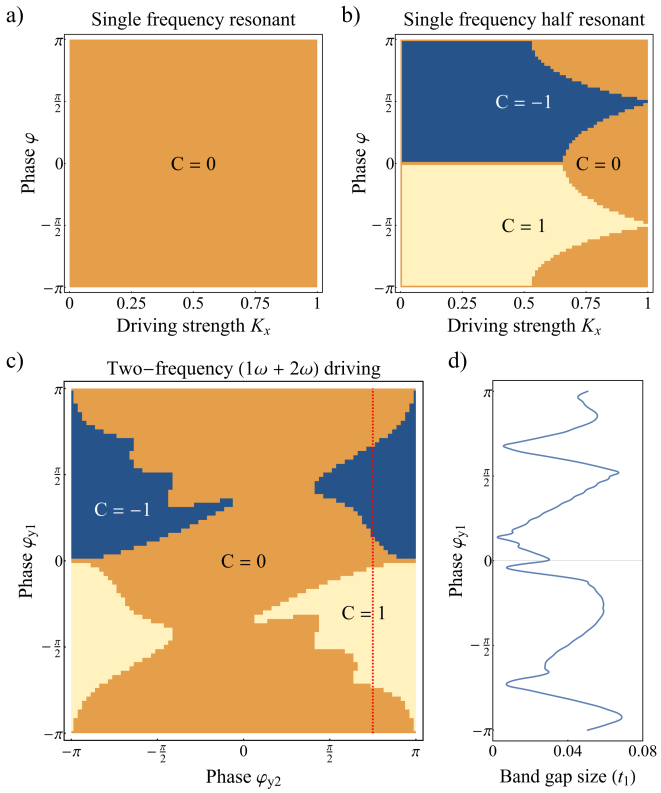

FIG. 3. Phase diagrams of the triangular lattice under resonant driving. Single-frequency driving on resonance ($\hbar\omega = 25.6t_1 = 1.28E_{rec}$, $K_y = 0.5$, $\varepsilon + \hbar\omega/2 \simeq 0$) leads to trivial bands (a), whereas driving on half-resonance ($\hbar\omega = 12.8t_1 = 0.64E_{rec}$, $K_y = 0.5$, $\varepsilon + \hbar\omega \simeq 0$) induces topological bands (b). The trivial regions in (b) are caused by bands being shifted out of resonance due to the *ac*-Stark effect. (c) shows the competition between the two resonant processes induced by the two-frequency driving with $K_{x1} = 0.4, K_{y1} = 0.5, K_{x2} = 0.02, K_{y2} = 0.02$. (d) resulting band gap evaluated for a cut through (c) along the red line.

in the effective Hamiltonian (Appendix C), leading to topologically non-trivial regions in the phase diagram (Fig. 3b, see also ref. [60]). Lines at $K_x = 0$ and $\varphi = 0$ have zero extent in the phase diagram of Fig. 3b, preventing the observation of a transition from $C \neq 0$ to $C = 0$ in a realistic experiment. While large driving amplitudes (beyond $K_x = 0.5$) render the model topologically trivial, this effect is not due to an interference between different processes, but rather due to the *ac*-Stark effect that shifts the bands out of resonance [4]. Combining the above two resonant schemes at 1ω and 2ω introduces genuine topological transitions as function of driving phase, as outlined in the following.

Two-frequency resonant elliptical driving. The competition between resonant 1ω and 2ω driving results in an interplay between topological phases with $C = 0$ and $C = \pm1$. We now consider the full two-tone waveforms of Eq. 4 for fixed $[K_{x1}, K_{x2}, K_{y1}, K_{y2}]$, and tuneable φ_{y1}

and φ_{y2} ($\varphi_{x2} = 0$). This Floquet scheme allows to cross topological transitions purely by changing the phase between 1ω and 2ω drives, as is evident from the distinct regions of $C = 0$ and $C \neq 0$ in the phase diagram (Fig. 3c). The values of the induced band gaps are on the order of 0.1 to 0.2 tunnelling energies, which can be enlarged by choosing stronger driving amplitudes.

Realising topological band structures in a Bravais lattice, such as the simple triangular lattice considered here, has important implications. For instance, it simplifies the generation of topological bands in the context of ultracold atoms. Up to now, two-dimensional topological models in optical lattices have been realised either in bipartite lattices [10, 12, 60], square lattices with moving superlattices [8, 9, 11], or by employing spin-orbit coupling [62]. These implementations rely on the relative phase stability between lattice or Raman laser beams, leading to a significant technological overhead. An insufficient phase stability may have been an obstacle for realising strongly correlated phases in two-dimensional topological lattices. The triangular lattice, on the contrary, can be built by simply superimposing three standing waves in the plane with no active stabilisation. Therefore, the 1ω–2ω Floquet scheme could provide an avenue towards realising correlated topological states of matter. In addition to its conceptual simplicity, the two-tone driving leads to the appearance of Berry curvature along a ring-shaped gap, which can be asymmetrically distributed (Fig. 2f), particularly in the topologically trivial regions of Fig. 3c. This supports a non-zero Berry curvature dipole, enabled by periodic driving, although the underlying lattice is trivial and inversion-symmetric. This finding is relevant beyond the field of ultracold atoms and it could enable the observation of nonlinear Hall effects which so far have relied on materials with broken inversion symmetry [63].

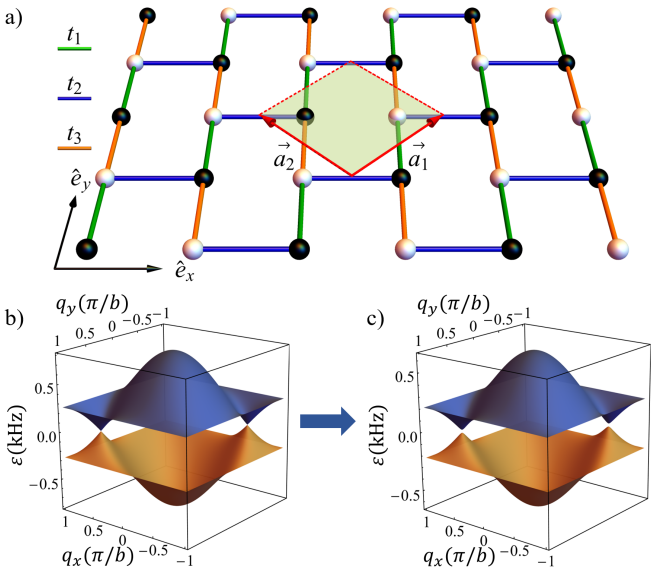

FIG. 4. Off-resonant driving in the hexagonal lattice (a) with tunnelings $t_1 = t_2 = t_3 = 0.06$ in units of E_{rec}. The static band structure features two degenerate Dirac points (b). Floquet driving lifts the degeneracy and opens a band gap (c) by effectively breaking symmetries.

IV. OFF-RESONANTLY DRIVEN HEXAGONAL LATTICE

The second application of the two-frequency driving method considers the hexagonal lattice in brick-wall configuration, shown in Fig. 4a. This potential can be realised in the same setup as the triangular lattice of sec. III, but the derivation also applies to 120° honeycomb lattices [12] as well as real graphene [17].

We start from the tight-binding Hamiltonian

$$\hat{H}_{\boldsymbol{q}}(\tau) = \left\{\sum_{i=1}^{3} t_i \cos\left[\mathbf{q}\cdot\mathbf{b}_i + \theta_i(\tau)\right]\right\}\sigma_x + \left\{\sum_{i=1}^{3} t_i \sin\left[\mathbf{q}\cdot\mathbf{b}_i + \theta_i(\tau)\right]\right\}\sigma_y, \tag{10}$$

The nearest-neighbour tunneling vectors are $\mathbf{b}_1 = (0,1)b$, $\mathbf{b}_2 = (-1,1)b$ and $\mathbf{b}_3 = (-1,0)b$ in the rotated coordinate system $\{\hat{e}'_x, \hat{e}'_y\}$ (Fig. 4a). The waveforms of Eq. 4 result in the following Peierls phases:

$$\begin{aligned}\theta_1(\tau) &= -K_{y1}\sin(\omega\tau + \varphi_{y1}) - K_{y2}\sin(2\omega\tau + \varphi_{y2}) = -\theta_3(\tau),\\ \theta_2(\tau) &= K_{x1}\sin(\omega\tau) + K_{x2}\sin(2\omega\tau + \varphi_{x2}),\end{aligned} \tag{11}$$

with the driving strengths being $K_{x1} = m\omega A_{x1}a/\hbar$, $K_{x2} = 2m\omega A_{x2}a/\hbar$, $K_{y1} = m\omega A_{y1}a/\hbar$, and $K_{y2} = 2m\omega A_{y2}a/\hbar$, as before. Since we do not consider interbanding couplings here, there is no need to apply unitaries and the high-frequency expansion can be directly conducted.

Single-frequency elliptical driving. The choice $K_{x2} = K_{y2} = 0$, $K_{x1} > 0$ corresponds to elliptical driving, giving rise to topological or trivial bands. For any $K_{y1} > 0$ and $\varphi_{y1} \mod \pi \neq 0$ we recover the well-known topological gap opening at both Dirac points due to time-reversal symmetry breaking (Fig. 4b-c) [64]. The limits of $K_{y1} = 0$ or $\varphi_{y1} \mod \pi = 0$ correspond to linearly polarised driving, leaving time-reversal symmetry intact and both Dirac points remain closed. However, the trivial region with $C = 0$ is only a 'line' of zero extent in the phase diagram (Fig. 5a, as before in Fig. 3b). Usually, a manifestly broken inversion symmetry of the underlying lattice is required to cross a topological phase transition and induce Haldane's 'parity anomaly', thereby extending the trivial 'lines' in the phase diagram to finite regions [2, 10]. In the following, we demonstrate that inversion symmetry can be broken by employing the two-tone Floquet drive only. Therefore, a topological phase transition between trivial and non-trivial regions can be achieved purely via driving.

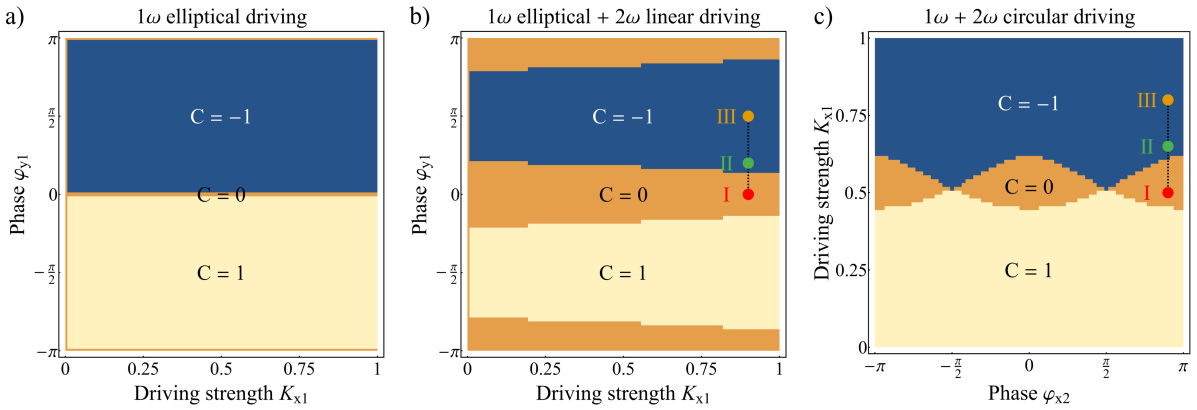

FIG. 5. Phase diagrams of the hexagonal lattice under off-resonant driving ($\hbar\omega = 20.8t_1 = 1.25E_{rec}$). Single-frequency elliptical driving ($K_{y1} = 0.9$, $K_{x2} = K_{y2} = 0$) can break time-reversal symmetry and result in a non-zero Chern number (a). The breaking of the inversion and time-reversal symmetries can be independently controlled by adding a linearly polarized field ($K_{y1} = K_{y2} = 0.9$, $K_{x2} = 0$ and $\varphi_{x2} = \varphi_{y2} = 0$) (b), as well as using two circular fields with opposite polarization ($K_{x1} = K_{y1}$, $K_{x2} = K_{y2} = 0.7$, $\varphi_{y1} = \pi/2$ and $\varphi_{y2} = \varphi_{x2} - \pi/2$) (c). The transition paths I - II - III marked in (b) and (c) correspond to the Lissajous curves in Fig. 1d-f and Fig. 1g-i, respectively.

Two-frequency driving. Starting from the above case of single-frequency elliptical driving, we add linearly polarized 'light' by setting $K_{x2} = 0$ while $K_{y2} \neq 0$. The driving field further breaks inversion symmetry and the competition between the breaking of inversion and time-reversal symmetry can be observed in Fig. 5b-c. The topological phase transition can simply be induced by tuning the phase along the marked path, corresponding to the Lissajous curves in Fig. 1d-f.

Alternatively, constraining $K_{x1} = K_{y1}$, $K_{x2} = K_{y2}$, $\varphi_{y1} = \pi/2$, and $\varphi_{y2} = \varphi_{x2} - \pi/2$ in Eq. 4, the $1\omega - 2\omega$ driving scheme corresponds to two counter-rotating, circularly polarized fields. Clearly, when one circular driving field is much larger than the other, the resulting Chern number will correspond to the helicity of the dominant field. However, when the amplitude of one circular field approaches the other one, the Lissajous curve becomes a 'cloverleaf' pattern and the breaking of time-reversal symmetry is suppressed (Fig. 1g-i). This competition allows to interpolate between topologically trivial and non-trivial settings (with either positive or negative mass terms) purely by changing driving phases. The resulting gap sizes are similar to the known results in the Haldane model [10]. Interestingly, we found that a pure Dirac Hamiltonian subject to two-frequency driving does not show a corresponding gap opening in the case of broken inversion symmetry. While time-reversal symmetry breaking via circular driving can be captured within the approximate Dirac Hamiltonian [17], the inversion symmetry breaking relies on the presence of a lattice potential. Mathematically, this can be seen from the fact that the driven Dirac Hamiltonian remains linear and its Fourier components at ω and 2ω will not mix in the high-frequency expansion. Conceptually, a specific driving pattern favours a gap opening specific to one sublattice of the honeycomb, which does not apply to the Dirac Hamiltonian.

We also studied the behaviour of inversion symmetry breaking beyond the validity of the high-frequency expansion, using numerically calculated band structures. Here, the gap opening scales roughly as $1/\omega^4$ which becomes dominant in the low-frequency regime. Therefore, the 1ω–2ω scheme could be particularly interesting for phase-controlled topological transitions in laser-driven graphene, which could be readily implemented in setups such as used in ref. [17].

V. CONCLUSION

We have shown that two-frequency Floquet driving in two dimensions gives rise to rich topological phase diagrams, both for resonant and off-resonant modulation. We identify the relative phase between the 1ω and 2ω drives as an important control parameter over the symmetry properties and the resulting topologies in the effective Floquet Hamiltonians. In many experiments, phase-only control is advantageous over other parameters, such as frequencies or amplitudes. For periodically driven real materials, such as graphene [17], incoherent excitations and electron relaxation can strongly affect the measurements, potentially obscuring any topological response. Incoherent effects often depend on the polarisation of the incident light, especially close to the contacts of a sample. Several of the driving schemes proposed in this work, particularly the case of counter-rotating, circular drives, depend only on the relative phase between the light fields. Therefore, we believe that our approach will

lead to novel applications in manipulation and detection of topological phenomena. By combining the schemes considered here with spin-dependent Floquet engineering [48], it may become possible to access the entire 'periodic table' of topological insulators [65].

ACKNOWLEDGMENTS

We acknowledge funding by the Swiss National Science Foundation (Grants No. 182650 and NCCR-QSIT) and European Research Council advanced grant TransQ (Grant No. 742579).

[1] K. v. Klitzing, G. Dorda, and M. Pepper, "New Method for High-Accuracy Determination of the Fine-Structure Constant Based on Quantized Hall Resistance," Phys. Rev. Lett. **45**, 494–497 (1980).
[2] F. D. M. Haldane, "Model for a Quantum Hall Effect without Landau Levels: Condensed-Matter Realization of the "Parity Anomaly"," Physical Review Letters **61**, 2015–2018 (1988).
[3] C. L. Kane and E. J. Mele, "Quantum Spin Hall Effect in Graphene," Phys. Rev. Lett. **95**, 226801 (2005).
[4] Martin Holthaus, "Floquet engineering with quasienergy bands of periodically driven optical lattices," Journal of Physics B: Atomic, Molecular and Optical Physics **49**, 013001 (2016).
[5] André Eckardt, "Colloquium: Atomic quantum gases in periodically driven optical lattices," Reviews of Modern Physics **89**, 11004 (2017).
[6] N. R. Cooper, J. Dalibard, and I. B. Spielman, "Topological bands for ultracold atoms," Reviews of Modern Physics **91**, 015005 (2019).
[7] Christof Weitenberg and Juliette Simonet, "Tailoring quantum gases by Floquet engineering," Nat. Phys. (2021), 10.1038/s41567-021-01316-x.
[8] M. Aidelsburger, M. Atala, M. Lohse, J. T. Barreiro, B. Paredes, and I. Bloch, "Realization of the Hofstadter Hamiltonian with Ultracold Atoms in Optical Lattices," Phys. Rev. Lett. **111**, 185301 (2013).
[9] Hirokazu Miyake, Georgios A. Siviloglou, Colin J. Kennedy, William Cody Burton, and Wolfgang Ketterle, "Realizing the Harper Hamiltonian with Laser-Assisted Tunneling in Optical Lattices," Phys. Rev. Lett. **111**, 185302 (2013).
[10] Gregor Jotzu, Michael Messer, Rémi Desbuquois, Martin Lebrat, Thomas Uehlinger, Daniel Greif, and Tilman Esslinger, "Experimental realization of the topological Haldane model with ultracold fermions," Nature **515**, 237–240 (2014).
[11] M. Eric Tai, Alexander Lukin, Matthew Rispoli, Robert Schittko, Tim Menke, Dan Borgnia, Philipp M. Preiss, Fabian Grusdt, Adam M. Kaufman, and Markus Greiner, "Microscopy of the interacting Harper–Hofstadter model in the two-body limit," Nature **546**, 519–523 (2017).
[12] N. Fläschner, D. Vogel, M. Tarnowski, B. S. Rem, D.-S. Lühmann, M. Heyl, J. C. Budich, L. Mathey, K. Sengstock, and C. Weitenberg, "Observation of dynamical vortices after quenches in a system with topology," Nature Physics **14**, 265–268 (2018).
[13] Karen Wintersperger, Christoph Braun, F. Nur Ünal, André Eckardt, Marco Di Liberto, Nathan Goldman, Immanuel Bloch, and Monika Aidelsburger, "Realization of an anomalous Floquet topological system with ultracold atoms," Nat. Phys. **16**, 1058–1063 (2020).
[14] Takashi Oka and Sota Kitamura, "Floquet Engineering of Quantum Materials," Annu. Rev. Condens. Matter Phys. **10**, 387–408 (2019).
[15] Mark S. Rudner and Netanel H. Lindner, "Band structure engineering and non-equilibrium dynamics in Floquet topological insulators," Nature Reviews Physics **2**, 229–244 (2020).
[16] Fenner Harper, Rahul Roy, Mark S. Rudner, and S.L. Sondhi, "Topology and Broken Symmetry in Floquet Systems," Annual Review of Condensed Matter Physics **11** (2020), 10.1146/annurev-conmatphys-031218-013721.
[17] J. W. McIver, B. Schulte, F.-U. Stein, T. Matsuyama, G. Jotzu, G. Meier, and A. Cavalleri, "Light-induced anomalous Hall effect in graphene," Nature Physics **16**, 38–41 (2020).
[18] Tomoki Ozawa, Hannah M. Price, Alberto Amo, Nathan Goldman, Mohammad Hafezi, Ling Lu, Mikael C. Rechtsman, David Schuster, Jonathan Simon, Oded Zilberberg, and Iacopo Carusotto, "Topological photonics," Reviews of Modern Physics **91**, 015006 (2019).
[19] Mikael C. Rechtsman, Julia M. Zeuner, Yonatan Plotnik, Yaakov Lumer, Daniel Podolsky, Felix Dreisow, Stefan Nolte, Mordechai Segev, and Alexander Szameit, "Photonic Floquet topological insulators," Nature **496**, 196–200 (2013).
[20] Zlata Fedorova, Haixin Qiu, Stefan Linden, and Johann Kroha, "Observation of topological transport quantization by dissipation in fast Thouless pumps," Nat Commun **11**, 3758 (2020).
[21] Romain Fleury, Alexander B Khanikaev, and Andrea Alù, "Floquet topological insulators for sound," Nat Commun **7**, 11744 (2016).
[22] Aravind Nagulu, Xiang Ni, Ahmed Kord, Mykhailo Tymchenko, Sasank Garikapati, Andrea Alù, and Harish Krishnaswamy, "Chip-scale Floquet topological insulators for 5G wireless systems," Nat Electron **5**, 300–309 (2022).
[23] Bing Chen, Shuo Li, Xianfei Hou, Feifei Ge, Feifei Zhou, Peng Qian, Feng Mei, Suotang Jia, Nanyang Xu, and Heng Shen, "Digital quantum simulation of Floquet topological phases with a solid-state quantum simulator," Photon. Res. **9**, 81 (2021).
[24] Kai Yang, Shaoyi Xu, Longwen Zhou, Zhiyuan Zhao, Tianyu Xie, Zhe Ding, Wenchao Ma, Jiangbin Gong, Fazhan Shi, and Jiangfeng Du, "Observation of Floquet topological phases with large Chern numbers," Phys. Rev. B **106**, 184106 (2022).
[25] M. Schiavoni, L. Sanchez-Palencia, F. Renzoni, and G. Grynberg, "Phase Control of Directed Diffusion in a Symmetric Optical Lattice," Phys. Rev. Lett. **90**, 094101 (2003).
[26] J. Struck, C. Ölschläger, M. Weinberg, P. Hauke, J. Simonet, A. Eckardt, M. Lewenstein, K. Sengstock, and P. Windpassinger, "Tunable Gauge Potential for Neutral

and Spinless Particles in Driven Optical Lattices," Physical Review Letters **108**, 225304 (2012).
[27] Tanay Nag, Robert-Jan Slager, Takuya Higuchi, and Takashi Oka, "Dynamical synchronization transition in interacting electron systems," Phys. Rev. B **100**, 134301 (2019).
[28] Philipp Stammer, Serguei Patchkovskii, and Felipe Morales, "Evidence of ac-Stark-shifted resonances in intense two-color circularly polarized laser fields," Phys. Rev. A **101**, 033405 (2020).
[29] Á. Jiménez-Galán, R. E. F. Silva, O. Smirnova, and M. Ivanov, "Lightwave control of topological properties in 2D materials for sub-cycle and non-resonant valley manipulation," Nat. Photonics **14**, 728–732 (2020).
[30] Christian Heide, Tobias Boolakee, Timo Eckstein, and Peter Hommelhoff, "Optical current generation in graphene: CEP control vs. $\omega + 2\omega$ control," Nanophotonics **10**, 3701–3707 (2021).
[31] Ofer Neufeld, Nicolas Tancogne-Dejean, Umberto De Giovannini, Hannes Hübener, and Angel Rubio, "Light-Driven Extremely Nonlinear Bulk Photogalvanic Currents," Phys. Rev. Lett. **127**, 126601 (2021).
[32] Kai-Xuan Yao, Zhendong Zhang, and Cheng Chin, "Domain-wall dynamics in Bose–Einstein condensates with synthetic gauge fields," Nature **602**, 68–72 (2022).
[33] Yuya Ikeda, Sota Kitamura, and Takahiro Morimoto, "Floquet engineering of electric polarization with two-frequency drive," Prog. Theor. Exp. Phys. , 04A101 (2022).
[34] Thaís V. Trevisan, Pablo Villar Arribi, Olle Heinonen, Robert-Jan Slager, and Peter P. Orth, "Bicircular Light Floquet Engineering of Magnetic Symmetry and Topology and Its Application to the Dirac Semimetal Cd 3 As 2," Phys. Rev. Lett. **128**, 066602 (2022).
[35] Sam Olin and Wei-Cheng Lee, "Topological phase transition in commensurate multi-frequency Floquet Su-Schrieffer-Heeger model," (2022).
[36] Chao Zhuang, Christopher R. Paul, Xiaoxian Liu, Samansa Maneshi, Luciano S. Cruz, and Aephraim M. Steinberg, "Coherent Control of Population Transfer between Vibrational States in an Optical Lattice via Two-Path Quantum Interference," Physical Review Letters **111**, 233002 (2013).
[37] Linxiao Niu, Dong Hu, Shengjie Jin, Xiangyu Dong, Xuzong Chen, and Xiaoji Zhou, "Excitation of atoms in an optical lattice driven by polychromatic amplitude modulation," Opt. Express **23**, 10064 (2015).
[38] Christopher Grossert, Martin Leder, Sergey Denisov, Peter Hänggi, and Martin Weitz, "Experimental control of transport resonances in a coherent quantum rocking ratchet," Nat Commun **7**, 10440 (2016).
[39] Frederik Görg, Kilian Sandholzer, Joaquín Minguzzi, Rémi Desbuquois, Michael Messer, and Tilman Esslinger, "Realization of density-dependent Peierls phases to engineer quantized gauge fields coupled to ultracold matter," Nature Physics (2019), 10.1038/s41567-019-0615-4.
[40] Konrad Viebahn, Joaquín Minguzzi, Kilian Sandholzer, Anne-Sophie Walter, Manish Sajnani, Frederik Görg, and Tilman Esslinger, "Suppressing Dissipation in a Floquet-Hubbard System," Physical Review X **11**, 011057 (2021).
[41] Kilian Sandholzer, Anne-Sophie Walter, Joaquín Minguzzi, Zijie Zhu, Konrad Viebahn, and Tilman Esslinger, "Floquet engineering of individual band gaps in an optical lattice using a two-tone drive," Phys. Rev. Research **4**, 013056 (2022).
[42] Alberto Castro, Umberto de Giovannini, Shusuke A. Sato, Hannes Hübener, and Angel Rubio, "Floquet engineering the band structure of materials with optimal control theory," (2022).
[43] Jin Hyoun Kang and Yong-il Shin, "Topological Floquet engineering of a one-dimensional optical lattice via resonant shaking with two harmonic frequencies," Physical Review A **102**, 063315 (2020).
[44] Joaquín Minguzzi, Zijie Zhu, Kilian Sandholzer, Anne-Sophie Walter, Konrad Viebahn, and Tilman Esslinger, "Topological Pumping in a Floquet-Bloch Band," Phys. Rev. Lett. **129**, 053201 (2022).
[45] Y H Wang, H Steinberg, P Jarillo-Herrero, and N Gedik, "Observation of Floquet-Bloch States on the Surface of a Topological Insulator," Science **342**, 453 (2013).
[46] Ankit S. Disa, Tobia F. Nova, and Andrea Cavalleri, "Engineering crystal structures with light," Nat. Phys. **17**, 1087–1092 (2021).
[47] Emil Vinas Boström, Martin Claassen, James McIver, Gregor Jotzu, Angel Rubio, and Michael Sentef, "Light-induced topological magnons in two-dimensional van der Waals magnets," SciPost Phys. **9**, 061 (2020).
[48] Gregor Jotzu, Michael Messer, Frederik Görg, Daniel Greif, Rémi Desbuquois, and Tilman Esslinger, "Creating State-Dependent Lattices for Ultracold Fermions by Magnetic Gradient Modulation," Phys. Rev. Lett. **115**, 073002 (2015).
[49] Jean Dalibard, "Réseaux dépendant du temps," Collège de France, Cours 4 (2013).
[50] Saar Rahav, Ido Gilary, and Shmuel Fishman, "Effective Hamiltonians for periodically driven systems," Phys. Rev. A **68**, 013820 (2003).
[51] N. Goldman and J. Dalibard, "Periodically Driven Quantum Systems: Effective Hamiltonians and Engineered Gauge Fields," Physical Review X **4**, 31027 (2014).
[52] André Eckardt and Egidijus Anisimovas, "High-frequency approximation for periodically driven quantum systems from a Floquet-space perspective," New Journal of Physics **17**, 093039 (2015).
[53] Marin Bukov, Luca D'Alessio, and Anatoli Polkovnikov, "Universal high-frequency behavior of periodically driven systems: from dynamical stabilization to Floquet engineering," Advances in Physics **64**, 139–226 (2015).
[54] Takahiro Mikami, Sota Kitamura, Kenji Yasuda, Naoto Tsuji, Takashi Oka, and Hideo Aoki, "Brillouin-Wigner theory for high-frequency expansion in periodically driven systems: Application to Floquet topological insulators," Phys. Rev. B **93**, 144307 (2016).
[55] H. F. Trotter, "On the Product of Semi-Groups of Operators," Proceedings of the American Mathematical Society **10**, 545–551 (1959), publisher: American Mathematical Society.
[56] Takahiro Fukui, Yasuhiro Hatsugai, and Hiroshi Suzuki, "Chern Numbers in Discretized Brillouin Zone: Efficient Method of Computing (Spin) Hall Conductances," Journal of the Physical Society of Japan **74**, 1674–1677 (2005).
[57] János K. Asbóth, László Oroszlány, and András Pályi, *A short course on topological insulators: band structure*

and edge states in one and two dimensions, Lecture notes in physics, Volume 919 (Springer, Cham, 2016).
[58] Stefan K. Baur, Monika H. Schleier-Smith, and Nigel R. Cooper, "Dynamic optical superlattices with topological bands," Phys. Rev. A **89**, 051605(R) (2014).
[59] Wei Zheng and Hui Zhai, "Floquet topological states in shaking optical lattices," Phys. Rev. A **89**, 061603(R) (2014).
[60] Shao-Liang Zhang and Qi Zhou, "Shaping topological properties of the band structures in a shaken optical lattice," Phys. Rev. A **90**, 051601(R) (2014).
[61] C. A. Bracamontes, J. Maslek, and J. V. Porto, "Realization of a Floquet-Engineered Moat Band for Ultracold Atoms," Phys. Rev. Lett. **128**, 213401 (2022).
[62] Wei Sun, Bao-Zong Wang, Xiao-Tian Xu, Chang-Rui Yi, Long Zhang, Zhan Wu, Youjin Deng, Xiong-Jun Liu, Shuai Chen, and Jian-Wei Pan, "Highly Controllable and Robust 2D Spin-Orbit Coupling for Quantum Gases," Phys. Rev. Lett. **121**, 150401 (2018).
[63] Z. Z. Du, Hai-Zhou Lu, and X. C. Xie, "Nonlinear Hall effects," Nat Rev Phys **3**, 744–752 (2021).
[64] Takashi Oka and Hideo Aoki, "Photovoltaic Hall effect in graphene," Phys. Rev. B **79**, 081406 (2009).
[65] Alexei Kitaev, "Periodic table for topological insulators and superconductors," in *AIP Conference Proceedings* (AIP, Chernogolokova (Russia), 2009) pp. 22–30.
[66] Thomas Uehlinger, Gregor Jotzu, Michael Messer, Daniel Greif, Walter Hofstetter, Ulf Bissbort, and Tilman Esslinger, "Artificial Graphene with Tunable Interactions," Physical Review Letters **111**, 185307 (2013).
[67] Nicola Marzari and David Vanderbilt, "Maximally localized generalized Wannier functions for composite energy bands," Phys. Rev. B **56**, 12847–12865 (1997).
[68] Ulf Bissbort, *Dynamical effects and disorder in ultracold bosonic matter*, Ph.D. thesis, Johann Wolfgang Goethe-Universität (2013).

Appendix A: Optical lattice potential

Lattices of various geometric configurations can be readily realised in the setup of ref. [66], that is,

$$\begin{aligned} &V_{\rm lat}(x,y) = \\ &-V_{\overline{x}}\cos(k_L x+\theta/2)^2 - V_x\cos(k_L x)^2 - V_y\cos(k_L y)^2 \\ &-2\sqrt{V_x V_y}\cos(k_L x)\cos(k_L y)\cos(\phi), \end{aligned} \tag{A1}$$

where $k_L = 2\pi/\lambda$. The spacing between neighbouring minima of a one-dimensional standing wave is $a = \lambda/2$, the recoil energy is $E_{rec} = (\hbar k_L)^2/(2m)$, the wavelength λ is 1064 nm, and the atoms are potassium-40. The following choice of parameters: $V_{\overline{x}} = 0.6$, $V_x = 0.3$, $V_y = 2.8$ all in units of E_{rec}, $\theta = \pi$, and $\phi = 0$ yields a triangular lattice. The hexagonal lattice can be realized by setting $V_{\overline{x}} = 12$, $V_x = 0.8$ and $V_y = 4.65$. Compared to the tight-binding lattices, we have the length of the unit cells $b = \sqrt{2}a = \lambda/\sqrt{2}$. The tight-binding parameters can be evaluated from the realistic lattice potential (Appendix B), yielding $t_1 = -0.05$, $t_2 = -0.07$, $t_3 = -0.07$, $\varepsilon = -0.66$ in units of E_{rec} (triangular lattice, $\eta_{sp} = 0.19$) and $t_1 = t_2 = t_3 = 0.06$ in units of E_{rec} (hexagonal lattice).

Appendix B: Derivation of the Hamiltonian

We start from Hamiltonian in co-moving frame,

$$\hat{H}_{cm}(\tau) = \frac{\hat{p}^2}{2m} + V_{lat}(\hat{r}) - \mathbf{F}(\tau)\cdot\hat{r}\ , \tag{B1}$$

where $\hat{p}$ and $\hat{r}$ are momentum and position operators, respectively, and $\mathbf{F} = -m\ddot{\mathbf{r}}_m(\tau) = -\dot{\mathbf{A}}(\tau)$. The Hamiltonian has two parts. The first two terms include the static lattice Hamiltonian and the last term represents a time-dependent dispersion.

Next, we expand $\hat{H}_{cm}(\tau)$ in Wannier basis [67],

$$w_{n,\mathbf{R}}(\mathbf{r}) \equiv w_n(\mathbf{r}-\mathbf{R}) = \frac{V}{(2\pi)^2}\int_{BZ} e^{-i\mathbf{k}\cdot\mathbf{R}}\phi_{n,\mathbf{k}}(\mathbf{r})\,d\mathbf{k}\ , \tag{B2}$$

where n is band index, $\phi_{n,\mathbf{k}}(\mathbf{r}) = e^{i\mathbf{kr}}u_{n,\mathbf{k}}(\mathbf{r})$ is Bloch state, $\mathbf{R} = n_1\mathbf{a}_1 + n_2\mathbf{a}_2$ is arbitrary lattice vector, and $\mathbf{a}_1$, $\mathbf{a}_2$ are primitive translation vectors in two dimensions.

In second quantization, we can rewrite the field operator in Wannier basis as

$$\hat{\psi}(\mathbf{r}) = \sum_{n,\mathbf{R}} w^*_{n,\mathbf{R}}(\mathbf{r})\hat{a}_{n,\mathbf{R}}\ , \tag{B3}$$

where $\hat{a}_{n,\mathbf{R}}$ is the annihilation operator.

The first part of the co-moving Hamiltonian can be expanded as

$$\hat{H}_0(\tau) = \sum_{n,m,\mathbf{R},\mathbf{R}'} \hat{a}^\dagger_{n,\mathbf{R}}\hat{a}_{m,\mathbf{R}'}\int w_{n,\mathbf{R}}(\mathbf{r})\left[\frac{\hat{p}^2}{2m} + V_{lat}(\hat{r})\right] w^*_{m,\mathbf{R}'}(\mathbf{r})\,d\mathbf{r}\ . \tag{B4}$$

Using the fact that the static Hamiltonian cannot mix different bands and the Wannier functions are exponentially localized, we only consider the onsite and nearest-neighbour couplings in individual bands,

$$\hat{H}_0(\tau) = \sum_{n,\mathbf{R}}\left\{\hat{a}^\dagger_{n,\mathbf{R}}\hat{a}_{n,\mathbf{R}}\varepsilon_n + \sum_{\mathbf{b}_i}\left[\hat{a}^\dagger_{n,\mathbf{R}}\hat{a}_{n,\mathbf{R}+\mathbf{b}_i}t_i + h.c.\right]\right\}\ , \tag{B5}$$

$$\varepsilon_n = \int w_{n,\mathbf{R}}(\mathbf{r})\left[\frac{\hat{p}^2}{2m} + V_{lat}(\hat{r})\right] w^*_{n,\mathbf{R}}(\mathbf{r})\,d\mathbf{r}\ , \tag{B6}$$

$$t_i = \int w_{n,\mathbf{R}}(\mathbf{r})\left[\frac{\hat{p}^2}{2m} + V_{lat}(\hat{r})\right] w^*_{n,\mathbf{R}+\mathbf{b}_i}(\mathbf{r})\,d\mathbf{r}\ . \tag{B7}$$

$\mathbf{b}_i = j\mathbf{a}_1 + k\mathbf{a}_2$ are the nearest-neighbour tunneling vectors. In the configuration of triangular and hexagonal lattices, $i \in \{1, 2, 3\}$. ε_n is the band center energy and t_i is the nearest-neighbour tunneling amplitude.

Now we consider the driving term which can couple different bands on-site but has negligible inter-site effects, i.e.

$$\begin{aligned}\hat{H}_1(\tau) &= -\sum_{n,m,\mathbf{R},\mathbf{R}'} \hat{a}^\dagger_{n,\mathbf{R}}\hat{a}_{m,\mathbf{R}'} \int w_{n,\mathbf{R}}(\mathbf{r})\,[\mathbf{F}(\tau)\cdot\hat{r}]\,w^*_{m,\mathbf{R}'}(\mathbf{r})\,d\mathbf{r} \\ &= -\sum_{n,\mathbf{R}} \hat{a}^\dagger_{n,\mathbf{R}}\hat{a}_{n,\mathbf{R}} \int w_{n,\mathbf{R}}(\mathbf{r})\,[\mathbf{F}(\tau)\cdot\hat{r}]\,w^*_{n,\mathbf{R}}(\mathbf{r})\,d\mathbf{r} - \sum_{n,m\neq n,\mathbf{R}} \hat{a}^\dagger_{n,\mathbf{R}}\hat{a}_{m,\mathbf{R}} \int w_{n,\mathbf{R}}(\mathbf{r})\,[\mathbf{F}(\tau)\cdot\hat{r}]\,w^*_{m,\mathbf{R}}(\mathbf{r})\,d\mathbf{r} \\ &= -\sum_{n,\mathbf{R}} \left[\hat{a}^\dagger_{n,\mathbf{R}}\hat{a}_{n,\mathbf{R}}\mathbf{F}(\tau)\cdot\mathbf{R} + \sum_{m\neq n} \hat{a}^\dagger_{n,\mathbf{R}}\hat{a}_{m,\mathbf{R}} a\mathbf{F}(\tau)\cdot\eta_{nm}\hat{r'}\right] .\end{aligned} \tag{B8}$$

Here we define the inter-band coupling as

$$\eta_{nm} = \frac{1}{b}\left|\int w_{n,\mathbf{R}}(\mathbf{r})\hat{r}w^*_{m,\mathbf{R}}(\mathbf{r})\,d\mathbf{r}\right| . \tag{B9}$$

By numerically evaluating η_{sp} according to the method in [66, 68], we justify that the dipole-like coupling term $\int w_{m,\mathbf{R}}(\mathbf{r})\hat{r}w^*_{n,\mathbf{R}}(\mathbf{r})\,d\mathbf{r}$ between s and p band is along the direction $\hat{r'} = \hat{r} = \hat{e}_x + \hat{e}_y$. In addition, we evaluate tunnelings and band center energies through calculating the Wannier functions of atoms in a realistic lattice potential.

The on-site driving term $\hat{a}^\dagger_{n,\mathbf{R}}\hat{a}_{n,\mathbf{R}}\mathbf{F}(\tau)\cdot\mathbf{R}$ breaks translation symmetry, so we need to rotate it away by applying the unitary

$$\hat{U}(\tau) = \exp\left(-i\sum_{\mathbf{R}n} \chi_{\mathbf{R}(\tau)}\hat{a}^\dagger_{n,\mathbf{R}}\hat{a}_{n,\mathbf{R}}\right), \tag{B10}$$

$$\hat{H}'(\tau) = \hat{U}^\dagger(\tau)\hat{H}(\tau)\hat{U}(\tau) - i\hbar\hat{U}^\dagger(\tau)\frac{\partial}{\partial\tau}\hat{U}(\tau), \tag{B11}$$

where $\chi_{\mathbf{R}}(\tau) = \frac{m}{\hbar}\mathbf{R}\cdot\dot{\mathbf{r}}_m(\tau)$. Then, transforming the Hamiltonian into quasi-momentum space and only considering the lowest two bands, we get the final Hamiltonian,

$$\hat{H}_{\mathbf{q}}(\tau) = \sum_{n\in\{s,p\}}\left\{\varepsilon_n\hat{a}^\dagger_n\hat{a}_n + \sum_{i=1}^{Z}\left[t_{n,i}\left(e^{i(\theta_i(\tau)+\mathbf{q}\cdot\mathbf{b}_i)}\hat{a}^\dagger_n\hat{a}_n + h.c.\right)\right] - \mathbf{F}(\tau)\cdot\hat{r}\sum_{m\in\{s,p\}\neq n}\eta_{nm}\hat{a}^\dagger_n\hat{a}_m\right\}, \tag{B12}$$

with the time-periodic Peierls phase $\theta_i(\tau) = \chi_{\mathbf{R}+\mathbf{b}_i}(\tau) - \chi_{\mathbf{R}}(\tau) = \frac{m}{\hbar}\mathbf{b}_i\cdot\dot{\mathbf{r}}_m(\tau)$.

Appendix C: Analytical Hamiltonian by the high-frequency expansion

In the following, we write down the effective Floquet Hamiltonian, analytically derived using the high-frequency expansion (HFE) in tight-binding approximation. The idea of the HFE is to decompose the original time-dependent Hamiltonian into Fourier components and obtain the effective Hamiltonians, then neglect the small high frequency terms. The effective Hamiltonian is decomposed into terms of different orders,

$$\hat{H}_{\text{eff}} = \sum_{n=0}^{\infty}\hat{H}^{(n)}_{\text{eff}}, \tag{C1}$$

which is in inverse power of ω, i.e. $\hat{H}^{(n)}_{\text{eff}} \sim \omega^{-n}$. If the frequency is much higher than other energy scales in the system, the high-order effective Hamiltonian can be truncated. Here we only use the first two orders [52],

$$\hat{H}^{(0)}_{\text{eff}} = \frac{1}{T}\int_0^T \hat{H}(\tau)\,d\tau \equiv \hat{H}_0 , \tag{C2}$$

$\hat{H}^{(0)}_{\rm eff}$	$\sigma_x\eta_{sp}\hbar\omega[K_x+K_y\cos(\varphi)]/2$
	$\sigma_y\eta_{sp}\hbar\omega K_y\sin(\varphi)/2$
	$\sigma_z\{\varepsilon+\hbar\omega/2+t_1\cos[(q_x-q_y)b]J_0(2K_x)+t_2\cos(q_xb)[J_0(K_x)J_0(K_y)-2J_1(K_x)J_1(K_y)\cos(\varphi)+2J_2(K_x)J_2(K_y)\cos(2\varphi)]+t_3\cos(q_yb)[J_0(K_x)J_0(K_y)+2J_1(K_x)J_1(K_y)\cos(\varphi)+2J_2(K_x)J_2(K_y)\cos(2\varphi)]\}$
$\hat{H}^{(1)}_{\rm eff,2}$	$\sigma_x\eta_{sp}\{-t_1\cos[(q_x-q_y)b]J_2(2K_x)[K_x+K_y\cos(\varphi)]-t_2\cos(q_xb)\{J_1(K_x)J_1(K_y)[K_y+K_x\cos(\varphi)]+J_0(K_y)J_2(K_x)[K_x+K_y\cos(\varphi)]+J_0(K_x)J_2(K_y)[K_y\cos(\varphi)+K_x\cos(2\varphi)]\}+t_3\cos(q_yb)\{J_1(K_x)J_1(K_y)[K_y+K_x\cos(\varphi)]-J_0(K_y)J_2(K_x)[K_x+K_y\cos(\varphi)]-J_0(K_x)J_2(K_y)[K_y\cos(\varphi)+K_x\cos(2\varphi)]\}\}/2$
	$\sigma_y\eta_{sp}\sin(\varphi)\{t_1\cos[(q_x-q_y)b]J_2(2K_x)K_y-t_2\cos(q_xb)\{J_1(K_x)J_1(K_y)K_x-J_0(K_y)J_2(K_x)K_y+J_0(K_x)J_2(K_y)[K_y+2K_x\cos(\varphi)]\}+t_3\cos(q_yb)\{J_1(K_x)J_1(K_y)K_x+J_0(K_y)J_2(K_x)K_y-J_0(K_x)J_2(K_y)[K_y+2K_x\cos(\varphi)]\}\}/2$
	$\sigma_z\eta^2\hbar\omega[K_x^2+K_y^2+2K_xK_y\cos(\varphi)]/8$

TABLE I. Effective Hamiltonian for the triangular lattice under single frequency driving resonant with the gap

$$\hat{H}^{(1)}_{\rm eff}=\frac{1}{\hbar\omega}\sum_{l=1}^{\infty}\frac{1}{l}\left[\hat{H}_l,\hat{H}_{-l}\right]=\sum_{l=1}^{\infty}\hat{H}^{(1)}_{{\rm eff},l}\ . \tag{C3}$$

Here, $\hat{H}_l$ are the Fourier components of the time-dependent Hamiltonian, $\hat{H}(\tau)=\sum_{l=-\infty}^{\infty}\hat{H}_l e^{il\omega\tau}$.

Table I is the effective Hamiltonian for the triangular lattice when the driving field is resonant with the gap energy. The constant terms are much larger than the quasimomentum dependent terms in off-diagonal, which means the on-site inter-band couplings are dominant. We safely neglect the Bessel functions higher than the second order as the driving strength $K\leq 1$ remains in weak driving regime.

Table II shows the case of single-frequency driving resonant with the half the gap. Now the off-diagonal terms are dominantly quasimomentum dependent. The Hamiltonian for the triangular lattice in two-frequency driving scheme are not listed here.

$\hat{H}^{(0)}_{\rm eff}$	$\sigma_z\{\varepsilon+\hbar\omega+t_1\cos[(q_x-q_y)b]J_0(2K_x)+t_2\cos(q_xb)[J_0(K_x)J_0(K_y)-2J_1(K_x)J_1(K_y)\cos(\varphi)+2J_2(K_x)J_2(K_y)\cos(2\varphi)]+t_3\cos(q_yb)[J_0(K_x)J_0(K_y)+2J_1(K_x)J_1(K_y)\cos(\varphi)+2J_2(K_x)J_2(K_y)\cos(2\varphi)]\}$
$\hat{H}^{(1)}_{\rm eff,1}$	$\sigma_x\eta_{sp}\{-t_1\sin[(q_x-q_y)b]J_1(2K_x)K_y\sin(\varphi)-t_2\sin(q_xb)\sin(\varphi)\{K_yJ_0(K_y)J_1(K_x)+K_xJ_1(K_y)J_2(K_x)-J_1(K_x)J_2(K_y)[K_y+2K_x\cos(\varphi)+2K_y\cos(2\varphi)]+J_0(K_x)J_1(K_y)[K_x+2K_y\cos(\varphi)]\}-t_3\sin(q_yb)\sin(2\varphi)\{K_yJ_0(K_x)J_1(K_y)+J_1(K_x)J_2(K_y)[K_x+2K_y\cos(\varphi)]\}\}$
	$\sigma_y\eta_{sp}\{t_1\sin[(q_x-q_y)b]J_1(2K_x)[K_x+K_y\cos(\varphi)]+t_2\sin(q_xb)\{J_0(K_y)J_1(K_x)[K_x+K_y\cos(\varphi)]-J_1(K_y)J_2(K_x)[K_y+K_x\cos(\varphi)]+J_1(K_y)J_0(K_x)[K_x\cos(\varphi)+K_y\cos(2\varphi)]-J_1(K_x)J_2(K_y)[K_x\cos(2\varphi)+K_y\cos(3\varphi)]\}+t_3\sin(q_yb)\sin(2\varphi)\{-J_0(K_y)J_1(K_x)[K_x+K_y\cos(\varphi)]-J_1(K_y)J_2(K_x)[K_y+K_x\cos(\varphi)]+J_1(K_y)J_0(K_x)[K_x\cos(\varphi)+K_y\cos(2\varphi)]+J_1(K_x)J_2(K_y)[K_x\cos(2\varphi)+K_y\cos(3\varphi)]\}\}$
	$\sigma_z\eta_{sp}^2\hbar\omega[K_x^2+K_y^2+2K_xK_y\cos(\varphi)]/4$
$\hat{H}^{(1)}_{\rm eff,3}$	$\sigma_x\eta_{sp}\{-t_2\sin(q_xb)\{K_xJ_1(K_y)J_2(K_x)+J_1(K_x)J_2(K_y)[K_y+2K_x\cos(\varphi)]\}+t_3\sin(q_yb)\{-K_xJ_1(K_y)J_2(K_x)+J_1(K_x)J_2(K_y)[K_y+2K_x\cos(\varphi)]\}\}/3$
	$\sigma_y\eta_{sp}\{t_2\sin(q_xb)\{J_1(K_y)J_2(K_x)[K_y+K_x\cos(\varphi)]+J_1(K_x)J_2(K_y)[K_y\cos(\varphi)+K_x\cos(2\varphi)]\}+t_3\sin(q_yb)\{J_1(K_y)J_2(K_x)[K_y+K_x\cos(\varphi)]-J_1(K_x)J_2(K_y)[K_y\cos(\varphi)+K_x\cos(2\varphi)]\}\}/3$
	$\sigma_z\eta_{sp}^2\hbar\omega[K_x^2+K_y^2+2K_xK_y\cos(\varphi)]/12$

TABLE II. Effective Hamiltonian for the triangular lattice under single frequency driving resonant with the half the gap

For the hexagonal lattice, Table III gives the general Hamiltonian under single-frequency off-resonant driving, while Table IV is the Hamiltonian under two-frequency off-resonant driving. Note that the second order Bessel functions are omitted in $\hat{H}^{(1)}_{\rm eff}$ in Table IV but kept in the numerical calculations.

$\hat{H}^{(0)}_{\text{eff}}$	$\sigma_x\{[t_1\cos(q_yb)+t_3\cos(q_xb)]J_0(K_{y1})+t_2\cos[(q_x-q_y)b]J_0(K_{x1})\}$ $\sigma_y\{[t_1\sin(q_yb)-t_3\sin(q_xb)]J_0(K_{y1})-t_2\sin[(q_x-q_y)b]J_0(K_{x1})\}$
$\hat{H}^{(1)}_{\text{eff}}$	$-\sigma_z\sum_{n=1}^{\infty}\frac{4}{n\hbar\omega}t_2J_n(K_{x1})J_n(K_{y1})\left[(-1)^{n+1}t_1\sin(q_xb)+t_3\sin(q_yb)\right]\sin(n\varphi_{y1})$

TABLE III. Effective Hamiltonian for the hexagonal lattice under single frequency off-resonant driving

$\hat{H}^{(0)}_{\text{eff}}$	$\sigma_x\{[t_1\cos(q_yb)+t_3\cos(q_xb)]J_0(K_{y1})J_0(K_{y2})+t_2\cos[(q_x-q_y)b]J_0(K_{x1})J_0(K_{x2})-$ $2[t_1\sin(q_xb)+t_3\sin(q_yb)]J_1(K_{y2})J_2(K_{y1})\sin(2\varphi_{y1}-\varphi_{y2})+2t_2\sin[(q_x-q_y)b]J_1(K_{x2})J_2(K_{x1})\sin(\varphi_{x2})\}$ $\sigma_y\{[t_1\sin(q_yb)-t_3\sin(q_xb)]J_0(K_{y1})J_0(K_{y2})-t_2\sin[(q_x-q_y)b]J_0(K_{x1})J_0(K_{x2})+$ $2[t_1\cos(q_xb)-t_3\cos(q_yb)]J_1(K_{y2})J_2(K_{y1})\sin(2\varphi_{y1}-\varphi_{y2})+2t_2\cos[(q_x-q_y)b]J_1(K_{x2})J_2(K_{x1})\sin(\varphi_{x2})\}$
$\hat{H}^{(1)}_{\text{eff}}$	$\sigma_z\frac{2}{3\hbar\omega}\{6J_0(K_{y2})J_1(K_{y1})[t_2J_1(K_{x1})J_1(K_{x2})(t_1\cos(q_xb)-t_3\cos(q_yb))\cos(\varphi_{x2}-\varphi_{y1})+(t_1^2-t_3^2)$ $J_1(K_{y1})J_1(K_{y2})\cos(2\varphi_{y1}-\varphi_{y2})]-6t_2J_0(K_{x2})J_1(K_{x1})[t_2J_1(K_{x1})J_1(K_{x2})\cos(\varphi_{x2})+J_1(K_{y1})J_1(K_{y2})$ $(t_1\cos(q_xb)+t3\cos(q_yb))\cos(\varphi_{y1}-\varphi_{y2})-J_1(K_{y1})J_0(K_{y2})(t_1\sin(q_xb)+t3\sin(q_yb))\sin(\varphi_{y1})]$ $-t_2J_1(K_{x2})J_1(K_{y2})[3J_0(K_{x1})J_0(K_{y1})(t_1\sin(q_xb)+t_3\sin(q_yb))\sin(\varphi_{x2}-\varphi_{y2})-2J_1(K_{x1})J_1(K_{y1})$ $(t_1\sin(q_xb)-t_3\sin(q_yb))(\sin(\varphi_{x2}-\varphi_{y1}-\varphi_{y2})+3\sin(\varphi_{x2}+\varphi_{y1}-\varphi_{y2}))]\}$

TABLE IV. Effective Hamiltonian for the hexagonal lattice under two frequency off-resonant driving